EJNMMI Physics

REVIEW Open Access

The SwiftScan step-and-shoot continuous mode improves SPECT scanning efficiency: a preliminary phantom and clinical test

Jicheng Li[1,2,3†], Kai Zhang[1,2,3†], Xingru Pang[1,2,3], Lele Huang[1,2,3], Xiaoxue Tian[1,2,3] and Jiangyan Liu[1,2,3*]

†Jicheng Li and Kai Zhang are co-first authors.

*Correspondence: ery_liujy@lzu.edu.cn

[1] Department of Nuclear Medicine, Lanzhou University Second Hospital, Lanzhou 730030, China
[2] Second Clinical School, Lanzhou University, Lanzhou 730030, China
[3] Key Laboratory of Medical Imaging of Gansu Province, Lanzhou 730030, China

Abstract

Purpose: The aim of the study was to investigate the value of SwiftScan Step-and-Shoot Continuous (SSC) scanning mode in enhancing image quality and to explore appropriate scanning parameters for reducing scan time.

Methods: This study was composed of a phantom study and two clinical tests. The differences in visual image quality scores, coefficient of variance (COV) of the background, image signal-to-noise ratio (SNR), contrast-to-noise ratio (CNR), and recovery coefficient (RC) of the sphere were compared between SSC mode and traditional Step-and-Shoot (SS) mode in the phantom study. Various "shoot" acquisition times (5s, 10s, 15s) and "step" angles (3-degree, 6-degree, 9-degree) were evaluated and verified. In the clinical tests, bone tomography and parathyroid tomography were performed on 30 patients each. Differences in visual image quality scores, background COV, image SNR, CNR, and standardized uptake value (SUV) of lesions were compared between the two modes.

Results: In the phantom study, SSC mode demonstrated higher visual scores and significantly reduced background COV ($P < 0.05$), and significantly increased SNR and CNR ($P < 0.05$) compared to SS mode. No significant alteration in RC was observed ($P > 0.05$). In the clinical tests, no significant differences were found between the optimal SSC scan combination (10s "shoot" and 6-degree "step")/ (10s "shoot" and 3-degree "step") and the traditional SS scan combination (15s "shoot" and 6-degree "step")/ (15s "shoot" and 3-degree "step") in visual image quality scores, background COV, image SNR, CNR, and SUV of bone and parathyroid high uptake lesions ($P > 0.05$).

Conclusion: The SwiftScan SSC mode can reduce acquisition time by 33% while maintaining similar image quality and quantification accuracy compared to SS mode. An SSC scanning protocol with a 10s "shoot" acquisition and 6-degree "step" or with a 10s "shoot" acquisition and 3-degree "step" over a 360-degree rotation, is recommended for clinical use.

Keywords: SwiftScan, Step-and-shoot continuous mode, SPECT/CT, Image quality, Acquisition efficiency

Introduction

In recent years, the scanning speed of Positron Emission Tomography (PET) has improved significantly [1, 2]. However, Single Photon Emission Computed Tomography (SPECT) scanning speed remains relatively slow compared to PET. Although a whole-body 99mTc-HMDP scan can be completed in under 20 min with a general-purpose CZT-based SPECT scanner, the cost of the scanner remains prohibitive for most hospitals [3]. A typical SPECT bone scan usually requires 20–30 min, including anterior and posterior whole-body scintigrams and regional tomography [4]. This extended scan time limits patient throughput, reduces patient comfort and compliance, and may result in patient movement.

The traditional SPECT acquisition mode for tomography is known as Step-and-Shoot (SS). In this mode, projection data are collected only when the detectors are stationary, which limits acquisition efficiency. In 1996, a Step-and-Shoot Continuous (SSC) mode has been introduced, allowing data to be acquired both when the detectors are stationary and while they move from one projection to the another [5]. Following this development, GE Healthcare launched the SwiftScan solution, which integrated a new low-energy, high-resolution sensitivity collimator with SSC acquisition mode. Reports indicate that SwiftScan achieves higher sensitivity while maintaining spatial resolution compared to conventional SPECT systems [6, 7]. Additionally, Bailly et al. demonstrated that the SwiftScan SSC mode can reduce acquisition time by 25% without compromising image quality [8].

However, few studies have evaluated the impact of the SwiftScan SSC mode in both phantom and clinical settings simultaneously, and the optimal scanning parameters for the SwiftScan SSC mode in clinical applications require further investigation. The purpose of this study was to assess the impact of the SwiftScan SSC mode in both phantom and clinical applications. Additionally, this study aimed to identify optimal scanning parameters for the SwiftScan SSC mode in clinical applications.

Materials and methods

Phantom experiment

Phantom preparation

The PET NEMA/IEC phantom was utilized for the phantom study. This phantom consists of a refillable body and six refillable spheres with internal diameters of 37 mm, 28 mm, 22 mm, 17 mm, 13 mm, and 10 mm, respectively. All spheres were filled with pertechnetate solution at a concentration of 165.5 kBq/ml, with a sphere-to-background concentration ratio of 8:1.

Data acquisition

SPECT data were acquired using the Discovery NM/CT 860 (GE HealthCare, Milwaukee, USA) in both SSC and SS modes. Various combinations of "shoot" acquisition times (5-s/10-s/15-s, abbreviated as 5s/10s/15s) and "step" angles (3-degree/6-degree/9-degree, abbreviated as 3d/6d/9d) were employed for a 360-degree rotation. A total of 18 data combinations were acquired, designated as: SS-5s-3d, SSC-5s-3d, SS-10s-3d, SSC-10s-3d, SS-15s-3d, SSC-15s-3d, SS-5s-6d,

SSC-5s-6d, SS-10s-6d, SSC-10s-6d, SS-15s-6d, SSC-15s-6d, SS-5s-9d, SSC-5s-9d, SS-10s-9d, SSC-10s-9d, SS-15s-9d, and SSC-15s-9d. For instance, SSC-15s-9d represents a combination of 15-s "shoot" and 9-degree "step" in the SSC mode acquisition.

The main energy window was set at $140 \pm 10\%$ KeV, with a scattering energy window of $120 \pm 5\%$ KeV. The phantom was positioned at the center of the field-of-view and scanned with body contour, using a matrix size of 128×128 and a zoom factor of 1.

CT data were acquired following each SPECT scan with a tube voltage of 120 kV and automatic tube current modulation in the longitudinal direction (current range 80–230 mA, noise index 14.2). The CT matrix size was 512×512, with a slice thickness of 1.25 mm.

Image processing and analysis

SPECT data were reconstructed using Q.Volumetrix MI Software on a Xeleris 4DR Process & Review Workstation (GE HealthCare, Milwaukee, USA) with the Ordered Subset Expectation Maximization (OSEM) algorithm, using 2 iterations and 10 subsets. Point spread function correction (Resolution Recovery, RR), CT-based Attenuation Correction (CTAC), and dual energy Scatter Correction (SC) were applied. A Butterworth post-filter was used with a critical frequency of 0.48 and a power of 10.

The reconstructed data were analyzed using Q.Volumetrix MI Software according to the National Electrical Manufacturers Association (NEMA) NU 2–2018 protocol. Circular regions-of-interest (ROIs) were delineated on the spheres in the center slice of the CT image along the inner edge of the spheres, as shown in Fig. 1A. For each sphere, 12 additional ROIs were copied to the background, positioned 15 mm away from the phantom edge and at least 15 mm apart from each other in the center slice. These ROIs were then copied to slices at $+2$ cm, $+1$ cm, -1 cm, and -2 cm relative to the center slice. Consequently, a total of 60 background ROIs were created for each sphere. This is illustrated in Fig. 1B (37-mm diameter sphere) and Fig. 1C (all spheres) for the center slice.

The Coefficient of Variance (COV) of the background for each sphere j was calculated using Eq. 1,

$$\mathrm{COV}_{B\mathrm{mean},j} = \frac{\sum_{i=1}^{60} Std_{Bi,j} / C_{Bi,j}}{60} \tag{1}$$

where $\mathrm{COV}_{B\mathrm{mean},j}$ was the mean value of the COV in the 60 background ROIs of sphere j; $\mathrm{Std}_{Bi,j}$ was the standard deviation of counts in the i-th background ROI of sphere j, and $C_{Bi,j}$ was the mean value of the counts in the i-th background ROI of sphere j.

The Signal-to-Noise Ratio (SNR) and the Contrast-to-Noise Ratio (CNR) were defined by the Eq. 2 and the Eq. 3, respectively [9, 10]

$$\mathrm{SNR}_j = \frac{C_{H,j}}{\mathrm{Std}_{B,j}} \tag{2}$$

$$\mathrm{CNR}_j = \frac{C_{H,j} - C_{B,j}}{\mathrm{Std}_{B,j}} \tag{3}$$

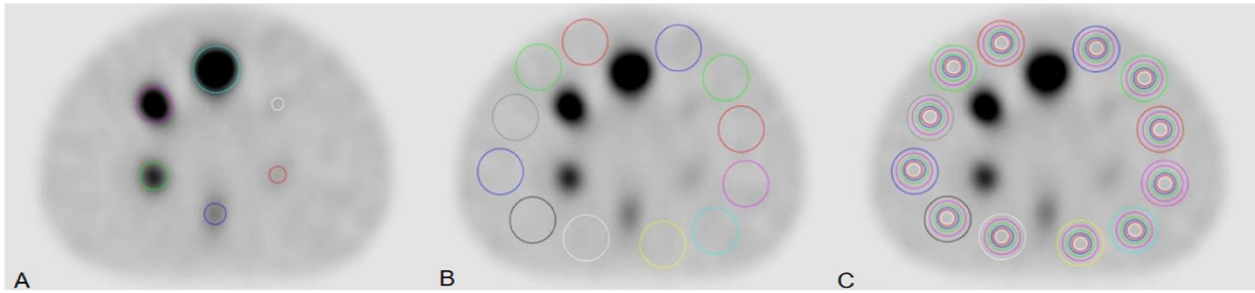

Fig. 1 **A**: Circular regions of interest (ROIs) were delineated on the spheres in the center slice of the CT image along the inner edge of the spheres, which were projected to the SPECT image. **B**: Each ROI was then copied to 12 ROIs in the background, so that the ROIs were 15 mm away from the phantom edge and no less than 15 mm away from each other in the center slice, and in the + 2 cm slice, + 1 cm slice, − 1 cm slice and − 2 cm slice. Hence, a total of 60 ROIs of each sphere were created in the background. The background ROIs of the 37-mm diameter sphere in the center slice were illustrated. **C**: The background ROIs of all spheres in the center slice were illustrated

where SNR_j and CNR_j was the SNR and CNR of sphere *j*, respectively; $C_{H,j}$ was the mean value of the counts in the sphere *j*; $Std_{B,j}$ was the mean value of standard deviation of counts in the 60 background ROIs for sphere *j*; $C_{B,j}$ was the mean value of the counts in the 60 background ROI of sphere j.

The Volumes of Interest (VOIs) were delineated for each sphere by a threshold of 40% on the SPECT image. The Recovery Coefficient (RC) of each sphere was defined by the Eq. 4,

$$RC_j = \frac{Ma_j}{Aa_j} \tag{4}$$

where the RC_j was the recovery coefficient of the sphere *j*; Ma_j was the uptake in the VOI of the sphere j; Aa_j was the decay corrected pertechnetate concentration in sphere *j* ($Aa_j = N_0.e^{-\lambda t}.N_0$ is the concentration of radioactivity at the beginning, λ is the decay constant, *t* is the decay time, e is approximately 2.71828).

Visual score of image quality

Image quality was scored blindly by one nuclear medicine physician with more than 15 years of experience, using a bipolar method. The main score was defined between 1 and 6, according to the number of spheres that could be identified. One point was given if only one sphere could be identified, two points if two spheres could be identified, and so on. The secondary score was determined according to the background noise level: 1 for high noise, 2 for medium noise, and 3 for low noise. The image quality was judged by the main score first, followed by the secondary score. The final image quality scores were sorted from poor to good as follows: 2-1, 2-2, 2–3, 3-1, 3-2, 3-3, 4-1, 4-2, 4-3, 5-1, 5-2, and 5-3.

Comparisons of quantitative data between the SSC and SS modes

The COV of background, SNR, CNR, and RC were compared between the 9 SSC combinations (SSC-5s-3d, SSC-10s-3d, SSC-15s-3d, SSC-5s-6d, SSC-10s-6d, SSC-15s-6d, SSC-5s-9d, SSC-10s-9d, and SSC-15s-9d) and the corresponding 9 SS combinations (SS-5s-3d, SS-10s-3d, SS-15s-3d, SS-5s-6d, SS-10s-6d, SS-15s-6d, SS-5s-9d, SS-10s-9d, and SS-15s-9d).

Comparisons of quantitative data between the SSC and SS modes in different size spheres

The COV of background, SNR, CNR, and RC were compared between the 9 SSC combinations and the corresponding 9 SS combinations in different size spheres.

Comparisons of SSC combinations with the traditional SS combinations

Comparisons of SSC-10s-6d and SSC-15s-9d with SS-15s-6d (traditional combination 1).

The COV of background, SNR, CNR, and RC of SSC-10s-6d, SSC-15s-9d, and SS-15s-6d were compared.

Comparisons of SSC-10s-3d and SSC-15s-6d with SS-15s-3d (traditional combination 2).

The COV of background, SNR, CNR, and RC of SSC-10s-3d, SSC-15s-6d, and SS-15s-3d were compared.

Verification in 4:1 contrast

Data analysis in Sect. "Comparisons of SSC combinations with the traditional SS combinations" were verified with a sphere-to-background concentration ratio of 4:1 (with pertechnetate solution at a concentration of 78.98 kBq/ml in the spheres).

SSC-10s-6d, SSC-15s-9d, SS-15s-6d, SSC-10s-3d, SSC-15s-6d, and SS-15s-3d combinations were acquired, respectively. The acquisition parameters and image processing methods of SPECT and CT were consistent with the 8:1 phantom study.

Statistical analysis

All the above comparisons were performed using paired-sample *t* tests with SPSS software (version 23, IBM).

Clinical experiment

Clinical design

Thirty patients with high-uptake bone metastases (10 prostate cancers, 4 breast cancers, 5 lung cancers, 3 liver cancers, and 8 colon cancers) and 30 patients with hypermetabolic parathyroid diseases (23 with hyperparathyroidism and 7 parathyroid tumors), scanned in our department from October 2023 to November 2024, were randomly enrolled. The mean age of bone tomography patients was 66 years (range: 20–78 years), and 43% were female. The mean age of parathyroid patients was 56 years (range: 27–72 years), and 66% were female. Fifteen of them were randomly selected for the combinations of SSC-10s-6d and SS-15s-6d (traditional combination 1), and the other 15 were used to perform the combinations of SSC-10s-3d and SS-15s-3d (traditional combination 2).

This study was approved by the Ethics Committee of the Second Hospital of Lanzhou University, and informed consent was obtained from all patients [2024A-799].

Data acquisition

All clinical data were acquired using a Discovery NM/CT 860 (GE Healthcare, Milwaukee, USA).

Following anterior–posterior whole-body bone scintigrams, two tomographic datasets were acquired in the largest high-uptake region in the bone clinical test. Patients were first scanned using the traditional combination SS-15s-6d/SS-15s-3d followed by a CT acquisition, then the SSC-10s-6d /SSC-10s-3d combination immediately without patient movement. The SPECT/CT scan protocol for the parathyroid test was consistent with that of the bone test, except for planar static imaging instead of the anterior–posterior whole-body scintigraphy.

The SPECT/CT scan protocol for both bone and parathyroid clinical tests was as follows: main energy window of SPECT 140 ± 10% keV; scatter energy window 120 ± 5% keV; matrix size 128 × 128; and zoom 1.0; use the body contour mode. The CT scan protocol was: tube voltage 120 kV; automatic tube current modulation in the longitudinal direction (current range 80–230 mA, noise index 14.2); matrix size 512 × 512; and slice thickness 1.25 mm.

Image processing and analysis

The processing and analysis methods for both bone and parathyroid clinical tests were consistent.

SPECT data were reconstructed using Q.Volumetrix MI Software on a Xeleris 4DR Process & Review Workstation (GE Healthcare, Milwaukee, USA) with the Ordered Subset Expectation Maximization (OSEM) algorithm (2 iterations, 10 subsets). Point spread function correction (Resolution Recovery, RR), CT-based Attenuation Correction (CTAC), and dual-energy Scatter Correction (SC) were applied. All CTAC corrections were based on the CT data acquired in the SSC-10s-6d combination. The post-filter was set to Butterworth, with a critical frequency of 0.48 and a power of 10.

A region of interest (ROI) was created in the central slice of the largest lesion in the SPECT image using a 40% threshold. The ROI was then copied to two nearby muscle regions as background ROIs.

The coefficient of variation (COV) of the background was defined by Eq. 5,

$$\mathrm{COV}_{B,L} = \frac{\sum_{i=1}^{2} \mathrm{Std}_{Bi,L} / C_{Bi,L}}{2} \tag{5}$$

where $\mathrm{COV}_{B,L}$ was the mean value of the COV in the 2 background ROIs; $\mathrm{Std}_{Bi,L}$ was the standard deviation of counts in the i-th background ROI of the patient, and $C_{Bi,L}$ was the mean value of the counts in the i-th background ROI.

The Signal-to-Noise Ratio (SNR) and the Contrast-to-Noise Ratio (CNR) were defined by the Eq. 6 and the Eq. 7, respectively,

$$\mathrm{SNR}_L = \frac{C_L}{\mathrm{Std}_{B\mathrm{mean,L}}} \tag{6}$$

$$\mathrm{CNR}_L = \frac{C_L - C_{B\mathrm{mean},L}}{\mathrm{Std}_{B\mathrm{mean},L}} \tag{7}$$

where $\mathrm{SNR}_{\mathrm{L}}$ and CNR_L was the SNR and CNR of the lesion, respectively; C_L was the mean value of the counts in the lesion; $\mathrm{Std}_{B\mathrm{mean},L}$ was the mean value of standard deviation of counts in the 2 background ROIs in the lesion; $C_{B\mathrm{mean},L}$ was the mean value of in the 2 background ROIs counts in the lesion.

The VOIs were delineated for each lesion using a threshold of 40% on the SPECT image. The mean values of the standardized uptake value (SUV) were measured based on the VOIs. These mean SUV values are referred to as SUV in this paper.

Visual score of image quality

The image quality of the SSC-10s-6d/SSC-10s-3d combination was blindly scored by two nuclear medicine physicians with more than 15 years of experience, using a 5-point scale, by comparing it with that of the traditional combination SS-15s-6d/SS-15s-3d. Scores of 1–5 were given when the image quality of the SSC-10s-6d/SSC-10s-3d combination was "much worse", "worse", "the same", "better", and "much better", respectively. The final score was the average of the scores from the two physicians.

Comparisons of quantitative data between SSC-10s-6d/SSC-10s-3d and SS-15s-6d/SS-15s-3d combinations

The coefficient of variation (COV) of the background, the signal-to-noise ratio (SNR), contrast-to-noise ratio (CNR), and the standardized uptake value (SUV) of the largest lesion in the SSC-10s-6d/SSC-10s-3d and SS-15s-6d/SS-15s-3d combinations were compared.

Statistical analysis

Comparisons of the visual scores, background COV, SNR, and SUV between the SSC-10s-6d/SSC-10s-3d and SS-15s-6d/SS-15s-3d combinations were performed using paired sample t-tests. The CNR between the SSC-10s-6d/SSC-10s-3d and SS-15s-6d/SS-15s-3d combinations was compared using the Friedman test [11]. All statistical analyses were performed using SPSS (version 23; IBM).

Results

Phantom experiment

Visual score of image quality

Visual scores are shown in Fig. 2. Nine combinations (SS-5s-3d, SSC-5s-3d, SS-5s-6d, SSC-5s-6d, SS-10s-6d, SS-5s-9d, SSC-5s-9d, SSC-10s-9d, and SS-10s-9d) scored lower than 4–1, while SSC-15s-3d scored up to 5–1. The remaining combinations (SS-10s-3d, SS-15s-9d, SSC-10s-6d, SSC-10s-3d, SSC-15s-9d, SS-15s-6d, SSC-15s-6d, and SS-15s-3d) scored between 4–1 and 4–3. With the same second "shoot" acquisition and degree "step" of a 360-degree rotation, the SSC modes had higher visual scores than the SS modes.

Comparisons of quantitative data between the SSC and SS modes

The background COVs of SSC combinations (0.18 ± 0.08, mean ± SD) were significantly lower than those of SS combinations (0.26 ± 0.22, $P < 0.05$). The SNR and CNR of SSC combinations (27.57 ± 23.21 and 19.21 ± 19.84) were significantly higher than those of SS combinations (21.55 ± 20.98 and 14.95 ± 17.48, respectively, both $P < 0.05$). The recovery coefficients (RCs) of SSC combinations (0.50 ± 0.36) were not significantly different from those of SS combinations (0.52 ± 0.37, $P > 0.05$). Detailed results are presented in Table 1.

Comparisons of quantitative data between the SSC and SS modes in different size spheres

The background COVs of the SSC combinations were significantly lower than those of the SS combinations for spheres with diameters larger than 17 mm ($P < 0.05$), while there were no significant differences for spheres with diameters less than or equal to 17 mm ($P > 0.05$). The SNRs and CNRs decreased with decreasing sphere diameter. The SNRs and CNRs of the SSC combinations were significantly higher than those of the SS combinations in almost all spheres ($P < 0.05$), except for the CNR in 13 mm diameter spheres ($P > 0.05$). The RCs were similar in both SSC and SS combinations ($P > 0.05$). The RCs in

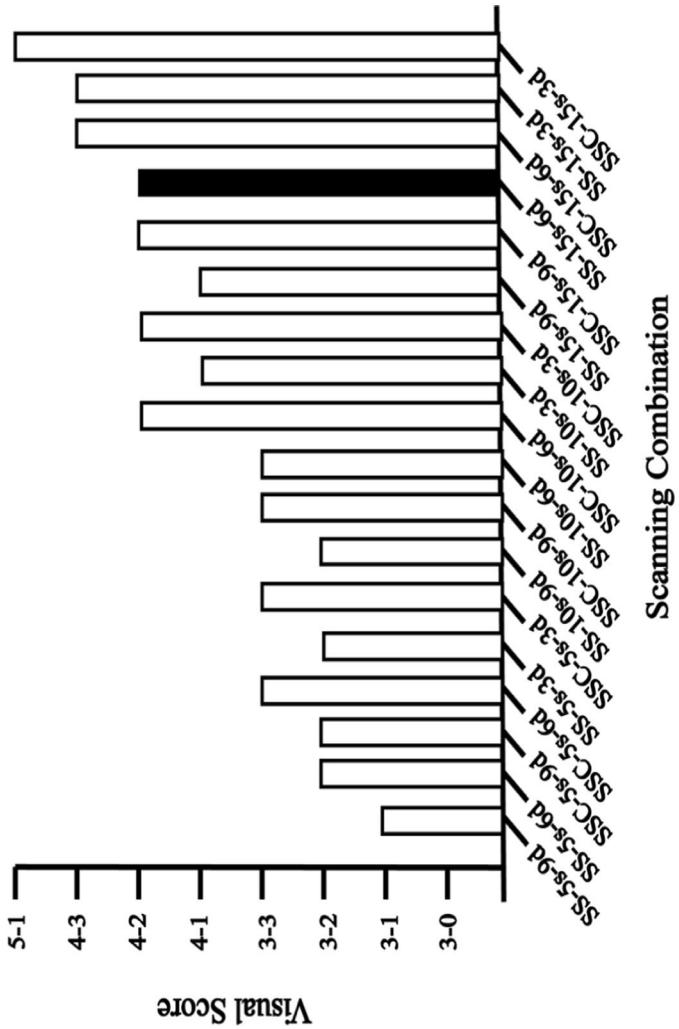

Fig. 2 Visual score of a physician of different acquisition combinations. Black parameter indicates conventional acquisition parameters

Table 1 Comparisons of quantitative data between the SSC mode and SS mode in the phantom study

Parameters	Mode	Mean	Std	T	P
COV	SS	0.26	0.22	5.124	0.001
	SSC	0.16	0.08		
SNR	SS	21.55	20.98	9.615	0.001
	SSC	27.57	23.21		
CNR	SS	14.95	17.48	− 7.313	0.001
	SSC	19.21	19.84		
RC	SS	0.52	0.37	1.591	0.118
	SSC	0.50	0.36		

37 mm and 28 mm diameter spheres were consistent with the actual concentrations. The RCs decreased with decreasing sphere diameter. Detailed results are presented in Fig. 3.

Comparisons of SSC combinations with the traditional SS combinations

Comparisons of SSC-10s-6d and SSC-15s-9d with SS-15s-6d (traditional combination 1).

There were no significant differences in background COV, SNR, CNR, and RC values between the SSC-10s-6d and SS-15s-6d combinations ($P > 0.05$). The SNR, CNR, and RC values of the SSC-15s-9d combination were significantly lower than those of the SS-15s-6d combination ($P < 0.05$), while the background COV value was significantly higher ($P < 0.05$). As the sphere diameter decreased, the background COV of the three combinations increased gradually, while the SNR, CNR, and RC values decreased gradually. The similar results was found in the 4:1 verification phantom. Detailed results are presented in Fig. 4.

Comparisons of SSC-10s-3d and SSC-15s-6d with SS-15s-3d (traditional combination 2).

It was also found that the background COV, SNR, CNR and RC values of the combination of SSC-10s-3d and SS-15s-3d had no statistical significance ($P > 0.05$). There were significant differences in COV, SNR, CNR and RC values between SSC-15s-6d and SS-15s-3d ($P < 0.05$), and similar results were found in the 4:1 verification phantom. The detailed results are shown in Fig. 5.

Clinical experiment

Visual score of image quality

In bone tomographic images, the visual score of the SSC-10s-6d/SSC-10s-3d combination was consistent with that of the SS-15s-6d/SS-15s-3d combination ($P > 0.05$). The visual scores of the SSC-10s-6d/SSC-10s-3d combination and the SS-15s-6d/SS-15s-3d combination in parathyroid tomographic images were also consistent ($P > 0.05$). Detailed results are presented in Table 2. An image example is shown in Fig. 6.

Comparisons of quantitative data between SSC and SS combinations

In bone tomographic images, there were no significant differences in background COV, SNR, CNR, and SUV values between the SSC-10s-6d/SSC-10s-3d and traditional

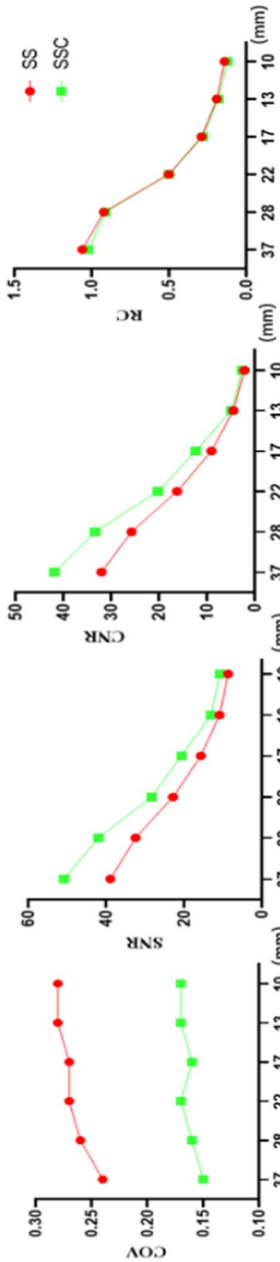

Fig. 3 Comparisons of quantitative data between the SSC and SS modes in different size spheres in the phantom study. **A**: The COVs of the background of the SSC combinations were lower than those of the SS combinations. **B**: The SNRs decreased with the decrease of the sphere diameter. The SNRs of the SSC combinations were higher than those of the SS combinations, but the differences became smaller with the decrease of the sphere diameter. **C**: The CNRs decreased with the decrease of the sphere diameter. The CNRs of the SSC combinations were higher than those of the SS combinations, but the differences became smaller with the decrease of the sphere diameter. **D**: The RCs were almost the same in both the SSC combinations and the SS combinations. The RCs in the spheres with the diameter of 37 mm and 28 mm spheres were basically consistent with the actual concentrations. The RCs decreased with the decrease of the sphere diameter

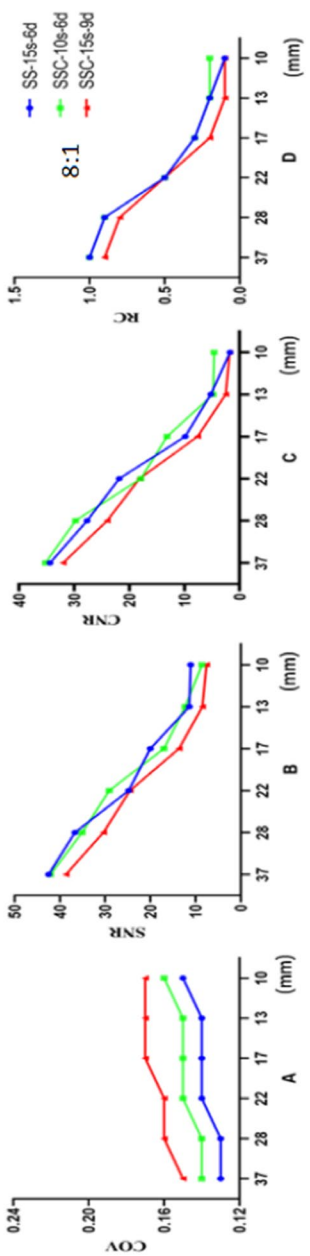

Fig. 4 The distributions of the quantitative data with different size spheres of SS-15S-6d, SSC-10s-6d and SSC-15s-9d combinations in the phantom study. Column A shows the distribution of the COV in the background; column B shows the SNR distribution; column C shows the CNR distribution, and column D shows the RC distribution. The first row shows the data with 8:1 (sphere-to-background concentration ratio) contrast; the second row shows the data with 4:1 contrast

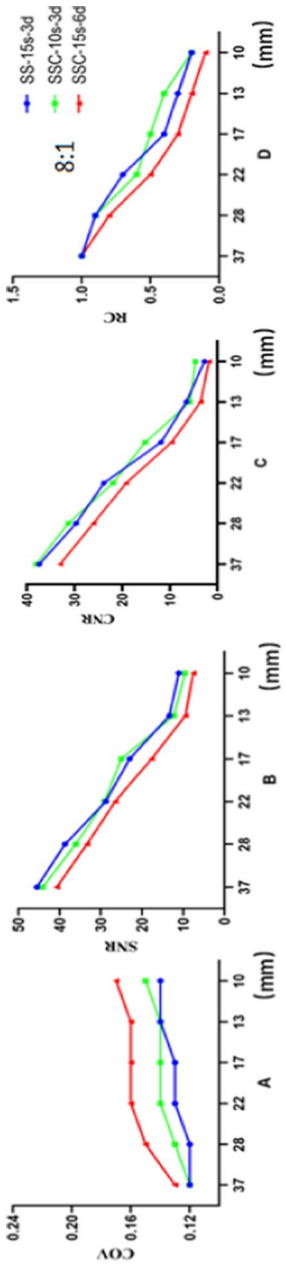

Fig. 5 The distributions of the quantitative data with different size spheres of SS-15S-3d, SSC-10s-3d and SSC-15s-6d combinations in the phantom study. Column A shows the distribution of the COV in the background; column B shows the SNR distribution; column C shows the CNR distribution, and column D shows the RC distribution. The first row shows the data with 8:1 (sphere-to-background concentration ratio) contrast; the second row shows the data with 4:1 contrast

Table 2 Comparisons of visual score and quantitative data between the SS and the SSC combinations in clinical tests

	Bone tomography				Parathyroid tomography			
Parameters	**Mode**	**Mean ± Std**	**T**	**P**	**Mode**	**Mean ± Std**	**T**	**P**
Visual score	SS-15s-6d	4.13 ± 0.83	0.222	0.827	SS-15s-6d	4.27 ± 0.80	0.764	0.458
	SSC-10s-6d	4.20 ± 0.86			SSC-10s-6d	4.07 ± 0.70		
	SS-15s-3d	4.62 ± 0.23	0.111	0.916	SS-15s-3d	4.77 ± 0.60	0.322	0.761
	SSC-10s-3d	4.55 ± 0.46			SSC-10s-3d	4.42 ± 0.55		
COV	SS-15s-6d	0.37 ± 0.13	−0.813	0.453	SS-15s-6d	0.29 ± 0.23	−0.617	0.345
	SSC-10s-6d	0.40 ± 0.07			SSC-10s-6d	0.31 ± 0.17		
	SS-15s-3d	0.26 ± 0.20	−0.311	0.979	SS-15s-3d	0.20 ± 0.33	−0.432	0.755
	SSC-10s-3d	0.32 ± 0.17			SSC-10s-3d	0.28 ± 0.19		
SNR	SS-15s-6d	156.89 ± 126.99	−0.52	0.614	SS-15s-6d	171.09 ± 134.91	−0.77	0.315
	SSC-10s-6d	213.67 ± 349.06			SSC-10s-6d	223.66 ± 301.21		
	SS-15s-3d	177.99 ± 133.99	−0.49	0.695	SS-15s-3d	199.16 ± 122.51	−0.43	0.712
	SSC-10s-3d	233.45 ± 270.11			SSC-10s-3d	246.33 ± 267.43		
SUV	SS-15s-6d	10.12 ± 2.40	0.218	0.836	SS-15s-6d	11.32 ± 2.70	0.188	0.719
	SSC-10s-6d	10.06 ± 2.52			SSC-10s-6d	11.21 ± 2.61		
	SS-15s-3d	14.22 ± 3.40	0.068	0.989	SS-15s-3d	15.44 ± 2.11	0.097	0.899
	SSC-10s-3d	13.35 ± 2.10			SSC-10s-3d	14.67 ± 2.01		

T test statistic, *P* asymptotic sig. (2-sided test)

combination SS-15s-6d/SS-15s-3d ($P > 0.05$). In parathyroid tomography images, there were no significant differences in background COV, SNR, CNR, and SUV between the SSC-10s-6d/SSC-10s-3d and traditional combination SS-15s-6d/SS-15s-3d ($P > 0.05$). Detailed results are presented in Tables 2 and 3.

Discussion

Low examination efficiency has been a persistent concern in SPECT/CT examinations. Recent technological advancements, including the development of CZT detectors and advanced reconstruction methods, offer promising solutions to this issue. Deng Xiangji proposed a model-driven deep learning method for SPECT reconstruction, aiming to combine the advantages of traditional algorithms with deep learning methods [12]. Xie Huidong et al. found that increasing angular sampling significantly improves image quality on the GE Discovery NM 530c/570c, while deep learning techniques can enhance reconstruction quality in stationary imaging [13]. Munir Ahmad et al. compared different regularization techniques used in emission tomographic imaging to improve resultant image quality [14]. These advanced image reconstruction technologies have demonstrated potential in reducing image noise and improving lesion recognition capabilities.

Data acquisition during detector rotation is a revolutionary technique in SPECT acquisition, with limited academic publications to date. Matsutomo N et al. found that the combination of different "step" and "shoot" parameters affected image quality and quantification accuracy in SPECT [15]. The impact of the SSC scan mode in various acquisition combinations and reconstruction methods requires further investigation in both phantom and clinical tests. This study aimed to investigate the effects of

Fig. 6 Comparison of patient images between conventional acquisition mode SS-15s-6d/SS-15s-3d and SSC-10s-6d/SSC-10s-3d. Where A1/A2 and a1/a2 are SS-15s-6d/SS-15s-3d and SSC-10s-6d/SSC-10s-3d modes for local bone tomography, and B1/B2 and b1/b2 are SS-15s-6d/SS-15s-3d and SSC-10s-6d/SSC-10s-3d modes for parathyroid tomography

Table 3 Comparisons of CNR between the SS and the SSC combinations in clinical tests

Parameters	Mode	25%	50%	75%	Z	P
Bone tomography	SS-15s-6d	18.04	40.19	98.26	− 1.572	0.116
	SSC-10s-6d	44.43	48.61	112.93		
	SS-15s-3d	21.02	48.32	108.11	− 0.971	0.421
	SSC-10s-3d	47.43	51.98	130.74		
Parathyroid tomography	SS-15s-6d	44.43	48.61	112.93	2.223	0.229
	SSC-10s-6d	61.91	70.77	144.41		
	SS-15s-3d	49.23	55.34	121.57	1.966	0.401
	SSC-10s-3d	66.95	82.24	163.43		

Z test statistic, *P* asymptotic sig. (2-sided test), %: percent

the GE SwiftScan SSC mode on image quality, noise, lesion detectability, and quantification accuracy in different "step and shoot" combinations through phantom and clinical studies.

In the phantom study, pharmaceutical concentrations in the spheres and their ratios to the background were determined based on clinical applications and data analysis feasibility [16, 17]. The study compared the coefficient of variation (COV) in the background, signal-to-noise ratio (SNR), contrast-to-noise ratio (CNR), and recovery coefficient (RC) values between SSC and SS modes. Results showed that the SSC mode had significantly lower background COV, higher SNR, and higher CNR compared to the SS mode, indicating improved image quality and lesion recognition ability. However, no significant difference was found in RC values, suggesting that the SSC mode did not impact quantitative of lesions. These findings are consistent with a recent study conducted in France [7]. The analysis identified that the improved volume sensitivity of the SwiftScan solution contributed to reduced noise in the images (leading to lower background variability), while at least maintaining equivalent contrast recovery and spatial resolution. Picone et al. also found that SUV quantification remained unchanged with the SSC acquisition mode [18].

SS-15s-6d and SS-15s-3d are both used as clinical routines. To explore whether any SSC combinations with shorter scan times can serve as replacements, several SSC combinations were selected for comparison. The results showed no statistical difference between SSC-10s-6d and SS-15s-6d, nor between SSC-10s-3d and SS-15s-3d. Therefore, SSC-10s-6d can replace SS-15s-6d, and SSC-10s-3d can replace SS-15s-3d.

To enhance the reliability of the study results, part of the phantom study was repeated using a sphere-to-background concentration ratio of 4:1. The results closely aligned with the previous findings from the 8:1 contrast. Therefore, it is reasonable to conclude that the results of this study can be applied to various lesions-to-background concentration ratios.

To verify whether SSC-10s-6d and SSC-10s-3d can replace SS-15s-6d and SS-15s-3d as new clinical routines. Thirty patients undergoing bone tomography and 30 patients undergoing parathyroid tomography were randomly enrolled in our clinical tests. Among these patients, 15 were assigned to SSC-10s-6d and SS-15s-6d acquisitions, while the other 15 received SSC-10s-3d and SS-15s-3d. The clinical experiment revealed no significant differences in background COV, image SNR, CNR, or

lesion SUV quantification between the SSC-10s-6d and SS-15s-6d combinations, nor between SSC-10s-3d and SS-15s-3d. These results indicate that the SSC acquisition mode can reduce the "shoot" time from 15 to 10s (approximately 33%) while maintaining similar image quality, lesion detectability, and quantification accuracy. This improvement can enhance patient throughput and comfort, consistent with findings reported by Valentin Picone et al. in a bone and lung SPECT study [18].

It is noteworthy that the image quality and quantitative accuracy of both SS and SSC modes decline as the sphere volume decreases. This is primarily due to the partial volume effect (PVE) and the inherent limitations in resolution associated with SPECT imaging, which particularly affect quantification accuracy for small volumes [5, 19–21]. Additionally, radioactive count attenuation calibration in phantom test and small sample sizes in each clinical test are noted as limitations. Future research should include a comprehensive investigation of all clinical applications, optimization of reconstruction parameters for SSC acquisition protocols, and exploration of the SSC mode's potential for reducing radiopharmaceutical doses.

Conclusions

The acquisition time of the SwiftScan can be reduced by 33% while maintaining similar image quality and quantification accuracy compared to the conventional SS mode. An SSC scanning protocol with a 10s "shoot" acquisition and 6-degree "step" can replace SS scanning protocol with a 15s "shoot" acquisition and 6-degree "step" rotation over 360 degrees mode, SSC scanning protocol with a 10s "shoot" acquisition and 3-degree "step" can replace SS scanning protocol with a 15s "shoot" acquisition and 3-degree "step" rotation over 360 degrees mode, both are recommended for bone tomography and parathyroid tomography.

Author contributions

J. Li and J. Liu contributed to the study conception and design. Material preparation, data collection, and analysis were performed by J. Li, K. Zhang,X. Pang,L. Huang, X. Tian. The first draft of the manuscript was written by J. Li, and all authors read and approved the final manuscript.

Funding

This work was financially supported by the Second Hospital of Lanzhou University, Youth Fund Project of Cuiying Science and Technology Innovation Program [grant number: CY2022-QN-A19], Science and Technology Department of Gansu Province, International Science and Technology Cooperation Project [grant number: 23YFMA0009], Science and Technology Department of Gansu Province Joint Research Fund Project [24JRRA922],Lanzhou University Second Hospital Cuiying Science and Technology Innovation Project [CY2023-MS-B10].

Availability of data and materials

The datasets analyzed during the current study are available from the corresponding author on reasonable request.

Declarations

Ethics approval and consent to participate

This article does not contain any experiments with animals. All procedures involving human participants were carried out in accordance with the ethical standards of the institutional and/or national research committee. This study was approved by the Ethics Committee of the Second Hospital of Lanzhou University [2024A-799].

Consent for publication

Written informed consent was obtained from all patients in the study.

Competing interests

The authors declare no competing interests. Conflict of interest there are no conflicts of interest to declare.

Received: 5 July 2024 Accepted: 12 December 2024
Published online: 02 January 2025

References

1. Zhang Y, Hu P, He Y, et al. Ultrafast 30-s total-body PET/CT scan: a preliminary study. Eur J Nucl Med Mol Imaging. 2022;49(8):2504–13. https://doi.org/10.1007/s00259-022-05838-1.
2. Hu Y, Liu G, Yu H, et al. Feasibility of acquisitions using total-body PET/CT with an ultra-low 18F-FDG activity. J Nucl Med. 2022;63(6):959–65. https://doi.org/10.2967/jnumed.121.262038.
3. Arvola S, Seppänen M, Timonen KL, et al. Detection of prostate cancer bone metastases with fast whole-body 99mTc-HMDP SPECT/CT using a general-purpose CZT system. EJNMMI Phys. 2022;9(1):85. https://doi.org/10.1186/s40658-022-00517-4.
4. Agency IAE. Clinical Applications of SPECT: New Hybrid Nuclear Medicine Imaging System. International Atomic Energy Agency (IAEA); 2008.
5. Cao Z, Maunoury C, Chen CC, Holder LE. Comparison of continuous step-and-shoot versus step-and-shoot acquisition SPECT. J Nucl Med Off Publ Soc Nucl Med. 1996;37:2037–40.
6. Shibutani T, Onoguchi M, Yoneyama H, et al. Performance of SwiftScan planar and SPECT technology using low-energy high-resolution and sensitivity collimator compared with Siemens SPECT system. Nucl Med Commun. 2021;42(7):732–7. https://doi.org/10.1097/MNM.0000000000001400.
7. Thibault F, Bailly M, Le Rouzic G, Metrard G. Clinical evaluation of general electric new Swiftscan solution in bone scintigraphy on NaI-camera: a head to head comparison with Siemens Symbia. PLoS ONE. 2019;14(9):e0222490. https://doi.org/10.1371/journal.pone.0222490.
8. Bailly M, Le Rouzic G, Metrard G, Ribeiro MJ. Faster acquisition for dopamine transporter imaging using swiftscan step and shoot continuous SPECT without impairing visual and semiquantitative analysis. Front Med. 2020;7:235.
9. Cherry SR, Sorenson JA, Phelps ME. What Is Nuclear Medicine? In: Physics in Nuclear Medicine. Elsevier; 2012. p. 1–6. https://doi.org/10.1016/B978-1-4160-5198-5.00001-0.
10. Huizing DMV, Sinaasappel M, Dekker MC, Stokkel MPM, de Witvan der Veen BJ. Lutetium SPECT/CT: evaluation of collimator, photopeak and scatter correction. J Appl Clin Med Phys. 2020;21(9):272–7. https://doi.org/10.1002/acm2.12991.
11. Rogasch JMM, Stefen IG, Hofheinz F, Grosser OS, Furth C, Mohnike K, et al. The association of tumor-to-background ratios and SUVmax deviations related to point spread function and time of-fight 18F-FDG-PET/CT reconstruction in colorectal liver metastases. EJNMMI Res. 2015;5:31.
12. Deng X. SPECT reconstruction algorithm based on Model-driven deep learning [D]. Guangdong University of Technology, 2022.
13. Xie H, Thorn S, Chen X, Zhou B, Liu H, Liu Z, Lee S, Wang G, Liu YH, Sinusas AJ, Liu C. Increasing angular sampling through deep learning for stationary cardiac SPECT image reconstruction. J Nucl Cardiol. 2023;30(1):86–100. https://doi.org/10.1007/s12350-022-02972-z.
14. Ahmad M, Shahzad T, Masood K, Rashid K, Tanveer M, Iqbal R, Hussain N, Shahid A. Local and non-local regularization techniques in emission (PET/SPECT) tomographic image reconstruction methods. J Digit Imaging. 2016;29(3):394–402. https://doi.org/10.1007/s10278-015-9853-x.
15. Matsutomo N, Takano E, Yamamoto T, Sato E. Continuous repetitive data acquisition with (123)I-FP-CIT SPECT: effects of rotation speed and rotation time. J Nucl Med Technol. 2019;47:319–25.
16. Bailey DL, Willowson KP. An evidence-based review of quantitative SPECT imaging and potential clinical applications. J Nucl Med. 2013;54(1):83–9.
17. Nakahara T, Daisaki SSC, Yamamoto Y, et al. Use of a digital phantom developed by QIBA for harmonizing SUVs obtained from the state-of -the-art SPECT/CT systems: a multicenter study. EJNMMI Res. 2017;7(1):53.
18. Picone V, Makris N, Boutevin F, Roy S, Playe M, Soussan M. Clinical validation of time reduction strategy in continuous step-and-shoot mode during SPECT acquisition. EJNMMI Phys. 2021;8(1):10. https://doi.org/10.1186/s40658-021-00354-x.
19. Alqahtani MM, Willowson KP, Constable C, Fulton R, Kench PL. Optimization of 99m Tc whole-body SPECT/CT image quality: a phantom study. J Appl Clin Med Phys. 2022;23(4):e13528. https://doi.org/10.1002/acm2.13528.
20. Erlandsson K, Buvat I, Pretorius PH, et al. A review of partial volume correction techniques for emission tomography and their applications in neurology, cardiology and oncology. Phys Med Biol. 2012;57(21):R119.
21. Leube J, Gustafsson J, Lassmann M, Salas-Ramirez M, Tran-Gia J. A deep-learning-based partial-volume correction method for quantitative 177Lu SPECT/CT imaging. J Nucl Med. 2024. https://doi.org/10.2967/jnumed.123.266889.

Publisher's Note